Delft University of Technology

Field test and numerical analysis of Insulated rail joints in heavy-haul railway

Xiao, Hong; Liu, Guangpeng; Yan, Dongwei; Zhao, Yue; Wang, Jiaqi; Wang, Haoyu

Important note
To cite this publication, please use the final published version (if applicable).
Please check the document version above.
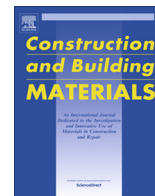
Field test and numerical analysis of Insulated rail joints in heavy-haul railway

Hong Xiao [a],*, Guangpeng Liu [a], Dongwei Yan [a], Yue Zhao [a], Jiaqi Wang [a], Haoyu Wang [b]

[a] *Beijing Key Laboratory of Track Engineering, Beijing Jiaotong University, Beijing 100044, China*
[b] *Engineering Structures Department, Delft University of Technology, the Netherlands*

HIGHLIGHTS

- Field investigation and tests were carried out at new IRJ and damaged IRJ.
- A 3D coupling model of heavy haul train-IRJ was established under different concave depths.
- Obtain the displacement distribution of different states at IRJs under the dynamic train load.
- Reveal the impact modes caused by different states of IRJs.

ARTICLE INFO

ABSTRACT

Insulated rail joints (IRJs) are widely used in heavy-haul lines, owing to they are safety critical components of track circuit. However, the IRJs breaks the continuity of the rail, making rail more vulnerable to damage under the long-term wheel-rail interaction. In order to study the performance of IRJs, field investigation and tests were carried out at new IRJ and damaged IRJ. At the same time, a 3D coupling model of heavy haul train-IRJ was established for the further analysis. The result shows that in regards to rail-surface regularity, the new IRJ and the damaged IRJ exhibits convex joint and concave joint respectively. IRJs will gradually turn to concave and dipped in the vicinity of end-post under long-term wheel-rail impact. Since there is a vertical rail displacement difference on both sides of the end-post between the two IRJs, causing the wheel-rail interaction has two different impact modes, of which one is downward height difference impact and the other is upward height difference impact. In normal speed, the impact caused by the damaged IRJ is larger than the new IRJ does and it leads to a severer damage to the whole track. The displacement of sleeper at the damaged IRJ is 7.6 times larger than at the new IRJ due to the void between the sleeper and the ballast. The transfer function of displacement from rail to sleeper at the new IRJ is between 0 and 0.4, while the damaged IRJ is between 0.42 and 6.1. The transfer function can be used as a vital index to evaluate the IRJ service state. With the increase of speed, the displacement of rail and sleeper at the two IRJs increases correspondingly. For the sake of decreasing the occurrence of fatigue damage and plastic deformation of rail and plate as much as possible, the maximum depth of concave should be reined within 0.55 mm.

1. Introduction

Joints are the weak links of rail lines. At present continuous welded rail (CWR) is widespread being used all over the world to ensure the smoothly running of trains. China is also mainly making use of CWR in the high-speed railways. However, on heavy-haul lines, the transmission of signal principally relies on track circuits which is composed of rails and IRJs, so IRJs are still irreplaceable in heavy-haul lines. Railway lines are divided into numerous circuit sections by IRJs to ensure the safe operation of trains [1]. When no trains pass through the signal section, the relay is cut off from underneath signal circuit and the light will turn green (Fig. 1(a)). When a train passes the section, the relay connects with the blow circuit and the light will turn red (Fig. 1(b)).

Although the high-stiffness glue and plates are been applied in the whole IRJs to maintain the overall rigidity of the IRJs, and a insulated end-post is been installed in the gap made it without obvious gap (Fig. 2). However, the end-post is usually made of nylon, fibre-glass or other polymer materials, whose elastic modu-

(a)No train passing through the electrical signal section

(b)A train passing through the electrical signal section
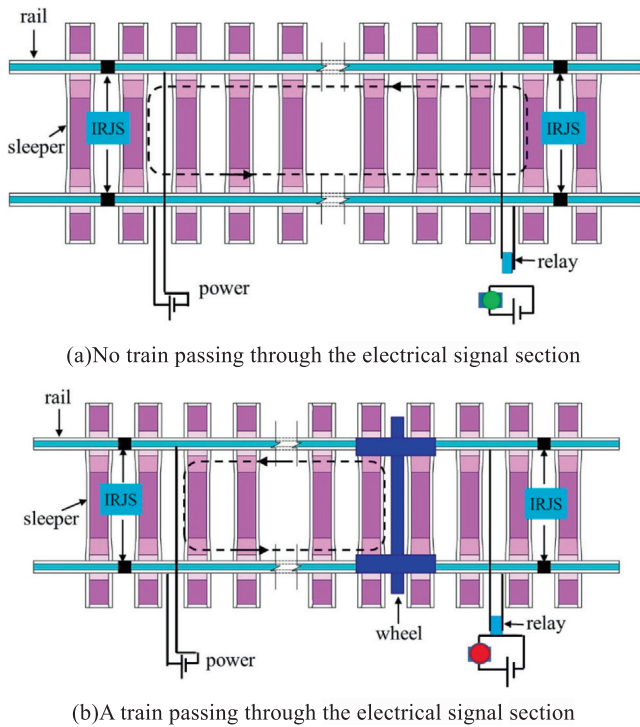
Fig. 1. The signal control principle of the IRJs.

Fig. 3. Damage of IRJs.

lus is only $1/1000 \sim 1/5$ of the rail [2], and the overall bending rigidity is only 2/3 of common rail section. As a result, it is easy causing a large impact force when a moving train passing through the IRJs [3]. Especially under the long-term impact of heavy-haul trains which has permitted heavy axle load, high freight capacity and track density, the damage of the IRJs are so prominent, greatly reducing its service life and increasing its maintenance costs [4].

Numerous modelling works has been carried out to research wheel-rail interaction in the vicinity of the IRJ. Mandal [5,6] employed rail as nonlinear isotropic/kinematic elastic–plastic material modelling, studied the stress and plastic strain around the railhead of end-post, finally he concluded that the railhead material fails due to alternating plasticity through low cycle fatigue. Emrecan et al. [7] evaluated different supporting and suspending joints on wood or concrete ties by a dynamic finite model, in the end, he reached that the supporting joints were better at reducing bar stress, especially on wood ties. Chen et al. [8] studied the normal and tangential contact stress distribution when a wheel
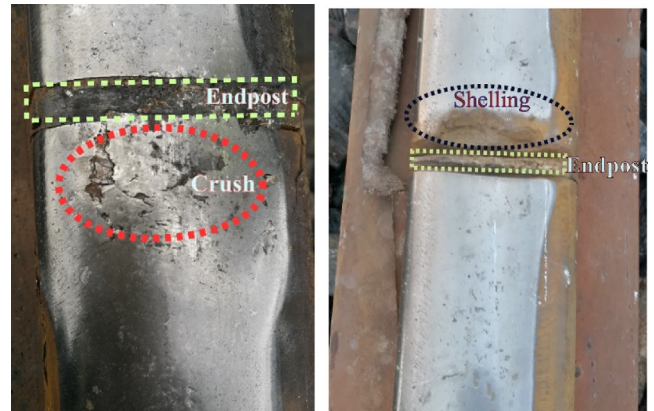
pass through IRJ. By building a sophisticated explicit finite element (FE)impact model and validated against a hammer test, Yang et al. [9,10] generalized that the wheel-rail interaction in the IRJs could reproduce high-frequency impact vibration and noise up to 10 kHz. Gallou et al. [11] established a 3D FE model of IRJs, analyzed the structural deflection performance of four different types of 4-bolted joints under a static load. Kaewunruen et al. [12] calculated a coupling of wave lengths between dipped rail joint and differential track settlements, found that some patterns of coupling irregularities could cause a significant reduction in dynamic impact factors. Sandstrom et al. [13] performed a series of numerical simulations, his research shows that the railhead edge at the insulation is severely strained and the main damage mechanism at IRJs was ratcheting effect, rather than low-cycle fatigue failure. Zong et al. [14] presents a dynamic wheel-rail contact impact modelling method for the determination of the impact loading, particularly analyzing the metallographic structure and residual stress of railhead surface of the damaged IRJs.

Field experiments is another effective approach to study dynamic behavior of IRJs, Askarinejad et al. [15,16] tested wheel-rail vertical impact force of different IRJs. Mayers [17] presented some results of a field test that was to investigate the train speed restrictions on the performance of IRJ, obtained the displacement of sleeper by integrating the acceleration. The way to calculate displacement through acceleration integration is easy to cause some frequency domain signals loss in the conversion process. Gallou et al. [18] measured the dynamic displacement of rail at IRJs by high-definition camera technology. Oregui et al. [19] discussed the frequency spectrum characteristics of IRJs in different states through plenty of field hammering tests. Molodova et al. [20],
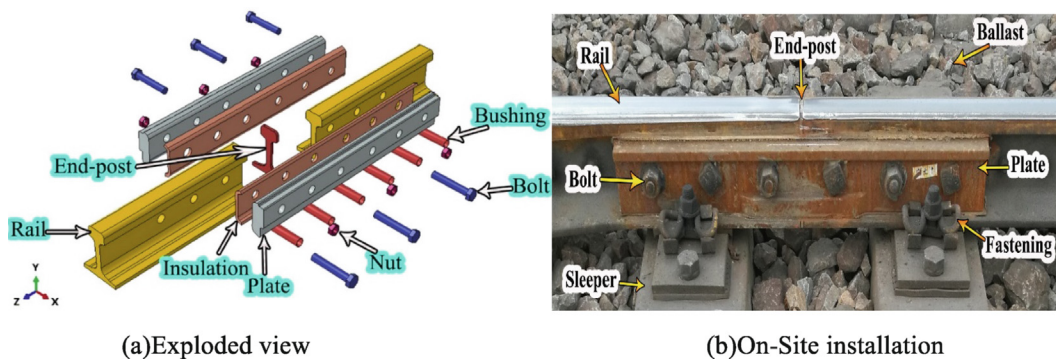

(a)Exploded view

(b)On-Site installation

Fig. 2. Schematic diagram of IRJs components.

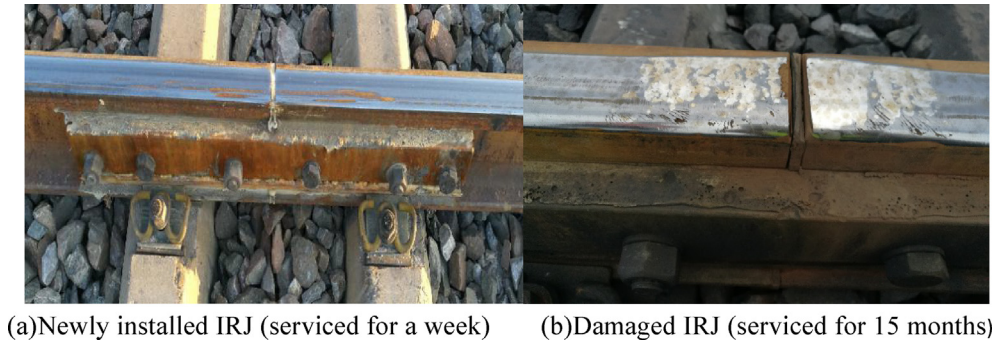(a)Newly installed IRJ (serviced for a week)   (b)Damaged IRJ (serviced for 15 months)
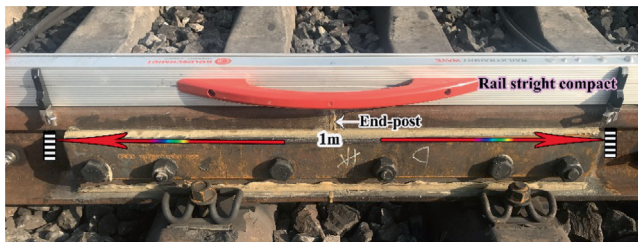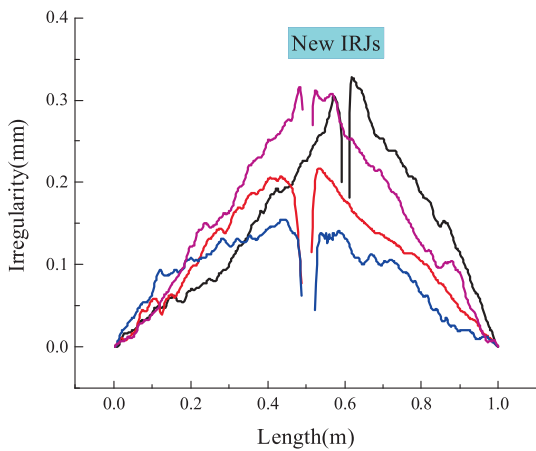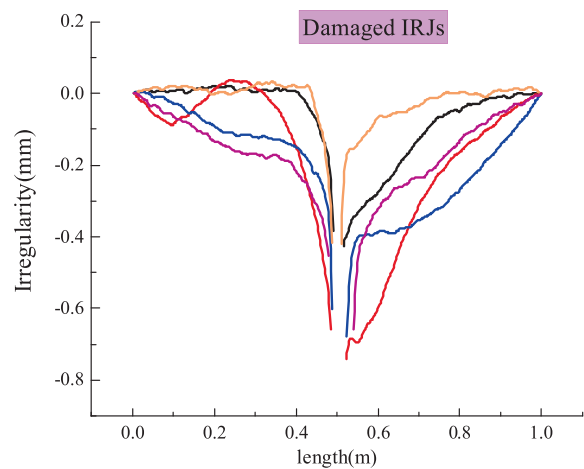
Fig. 4. Comparison of two different IRJs.

(a) Field test of IRJ irregularity

(b) Field test of four new IRJs irregularities

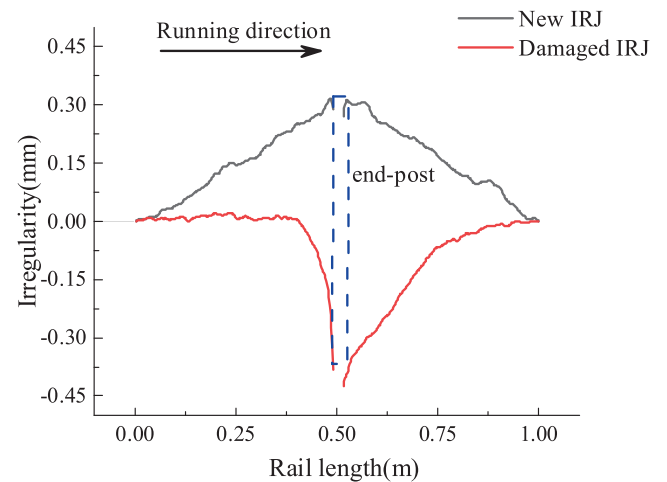(c) Field test of five damaged IRJs irregularities

Fig. 5. Comparison of regularities of IRJs.

(d)Irregularity results of two representative IRJs

Fig. 5 (continued)

reflected the vibration and impact characteristics of IRJs by testing acceleration of train axle box in the field. Xu [21] designed a reinforced joint used in heavy-haul railway, and compared the rail static deflection and plate stress at different joints by combining indoor test and FE analysis.

From the above research, it can be seen the majority of publications mainly focus on the wheel-rail dynamic force and vibration, only a paucity of work on the joint deformation under train dynamic load. As a matter of fact, the related maintenance specifications of IRJs currently only stipulate the threshold value of deformation such as rail joint surface irregularity, and there is no limit about stress. In addition, one of the major reasons for the large wheel-rail impact at IRJs is the existence of height difference and inflection angle. Therefore, in order to better shed light on the performance of IRJs, it is highly necessary to study rail displacement distribution around the end-post.

Based on what mentioned above, this paper selected a typical track section, with a new IRJ on one side of track centerline and a damaged IRJ on the other side, and carried out a series of field tests of rail surface regularity and dynamic displacement,
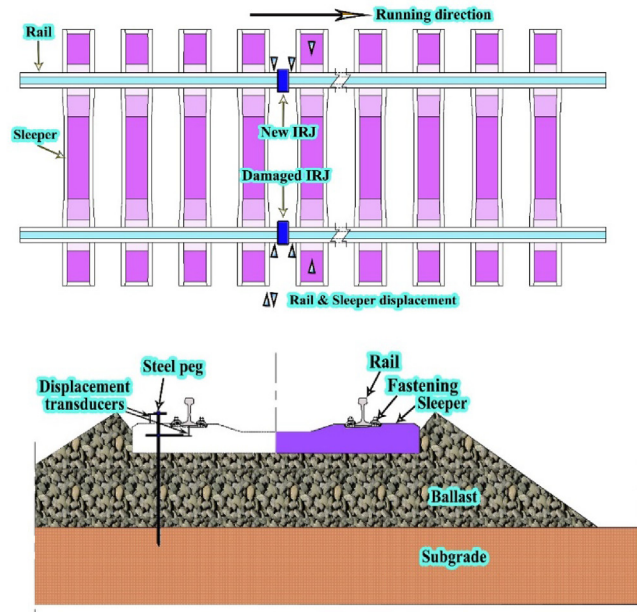
(a)Instruments layout   (b)Longitudinal section Instruments layout
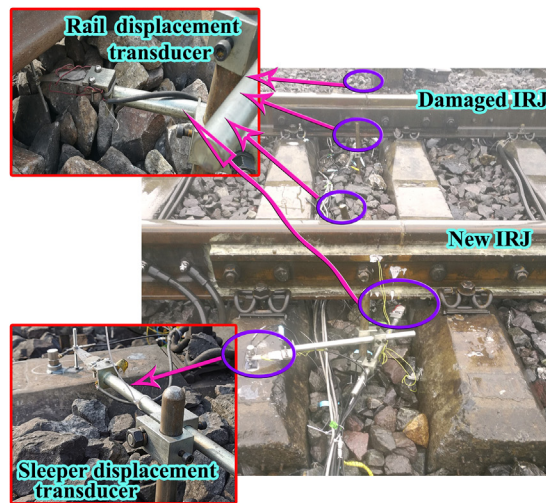
(c)Field instruments installation

Fig. 6. Field test layout.
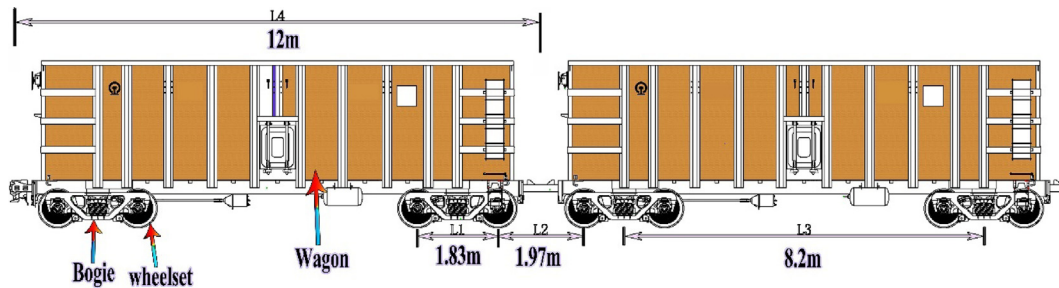
Fig. 7. Schematic diagram of C_{80} wagon.

obtained displacement distribution of different states at IRJs. Meanwhile a 3D coupled model of heavy haul train-rail joints was established for systematic theoretical analysis. The results can provide an important reference for revealing the behavior of IRJs, put forward joint maintenance measures and optimize structural design.

(a)Typical time history chart of rail displacement

(b)Typical displacement fluctuation when a wheel passing through IRJ

Fig. 8. Rail dynamic displacement at IRJs.

2. Field investigation of IRJs

Through a great deal of investigations on a most busy coal-transporting heavy-haul lines in china, it is found that the damage of IRJs in service are deadly serious, mainly as crushing of railhead, shelling, glue separation and other damages (Fig. 3).
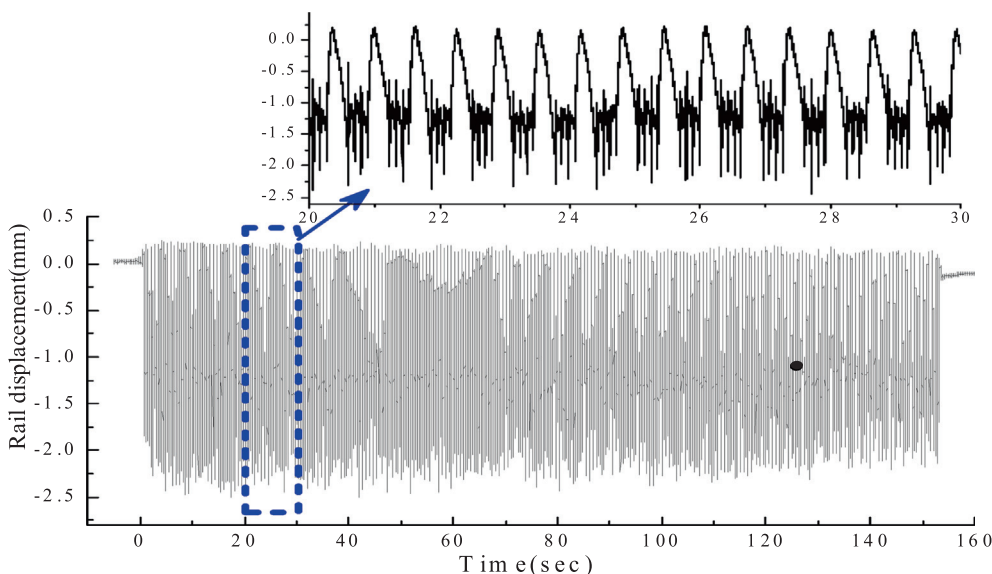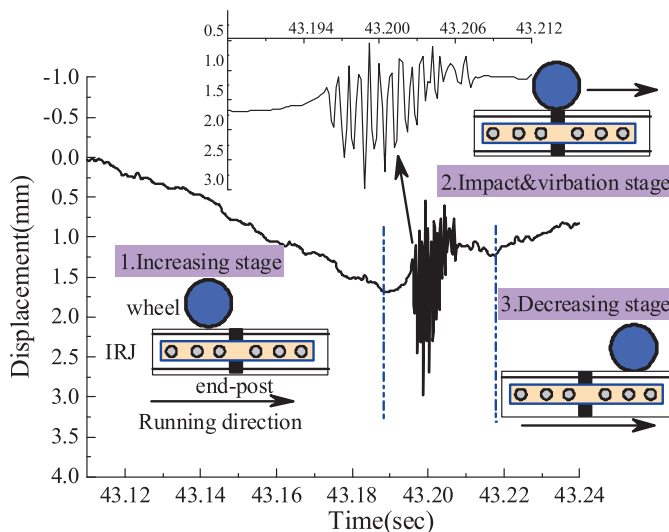
In order to reveal the performance of IRJs accurately, rail surface irregularity and dynamic tests were carried out in the field. The rail surface of the newly installed IRJ is intact (Fig. 4(a)), while the damaged IRJ railhead shows shelling (Fig. 4(b)). The rail is CHN75kg/m, whose sleeper spacing is 60 cm in ballasted track, generally located in a straight subgrade section. Moreover, the new IRJ has just been worked for a week, while the damaged IRJ has been in service for 15 months, with a total passing weight of about 560 million tonnes.

The irregularities of IRJs were obtained by Rail Straight Compact whose measuring length is 1 m, and its horizontal resolution is 500 testing points. The field test presented in Fig. 5(a), the irregularity

of new and damaged IRJs were showed in Fig. 5(b) Fig. 5(c), and two representative IRJs showed in Fig. 5(d).

Fig. 5(b)(c) illustrates the new IRJs presents a convex style, while the damaged IRJs appears concave. Therefore, a representative new IRJ and damaged IRJ (Fig. 5(d)) were been selected for conducted the following test.

In china, the acceptance standard for new installed IRJs stipulates that the maximum deflection of IRJs regularity is no less than 0.3 mm[22],and there is no maintenance standard for the damaged IRJs.

It can be seen from Fig. 5(d) that the irregularity of new IRJ shows convex, with the maximum convex deflection of rail reaching 0.3 mm which can meet the limit requirement[22], and the continuity of rail regularity on both sides of the end-post is smoothly. The damaged IRJ appears concave, whose rail is obvious dipped, concave and bending adjacent to the end-post, leading to a poor regularity. According to measured value, the maximum deflection depth of damaged IRJ is −0.43 mm. It is concluded that
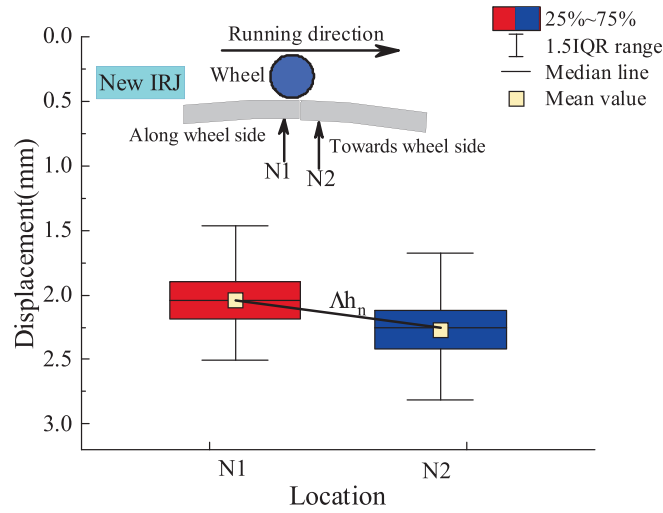
(a) Peak distribution of rail displacement at both ends of the new IRJ end-post
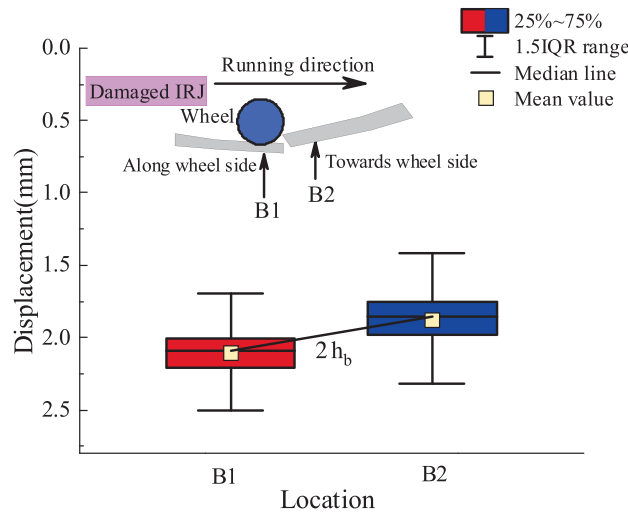
Fig. 9. The distribution of peak rail displacement at the two IRJs.
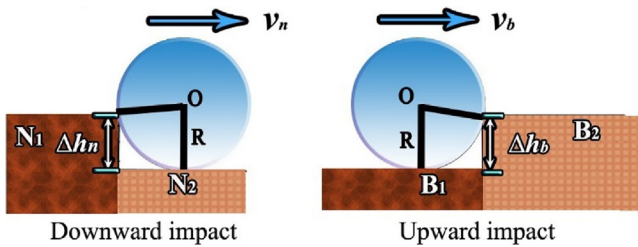
Fig. 10. Height Difference impact mode formed near the two IRJs.

the process of IRJs changing from new to old is also the process of joint regularity changing from convex to concave.

3. Field test arrangement

3.1. Test setup

Field dynamic tests and irregularity tests are conducted in the same section. The test arrangements mainly include displacement of rail and sleeper on both sides of end-post (Fig. 6(a)). Displacement transducers are fixed on steel pegs whose one ends reached
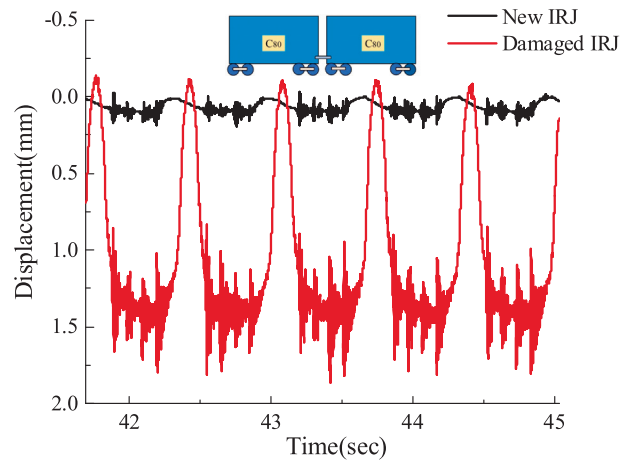
Fig. 11. Comparative analysis of dynamic displacement of sleepers.

on the subgrade, only in this way it can provide a no-moving reference (Fig. 6(b)). The whole signal acquisition system adopts the German integrated measurement & control (IMC for short) digital acquisition instrument. Field tests instruments of IRJs installed as shown in Fig. 6(c).

3.2. Introduction of test train

The vehicle mainly tested on-site is C$_{80}$ wagon with an axle load of 25 t. According to test requirements, on-site operating speed is mainly distributed between 10 and 70 km/h. The wagon is mainly composed of three parts: wheelset, bogie and car body. The wheelbase is L1, and adjacent wheelbase is L2, distance of the bogie is L3 and length of the car body is L4(Fig. 7).

4. Testing data

4.1. Rail displacement

Taking the rail displacement tested in the new IRJ as an example. The speed of heavy-haul train is 60 km/h. For the sake of data clearly displayed, 1/15 period of data was cut out from the whole 150 s data (Fig. 8(a)). Fig. 8(a) shows that each wheel passed through the measured section would arouse an obvious peak, and the dynamic load of train has prominent periodic influence on the rail displacement. When a wheel passed through endpost, its displacement exhibited three different stages (Fig. 8(b)): increasing stage, impact & vibration stage, decreasing stage, among this, the reason caused stage 2 is that difference of track state on both side of the end-post and the existence of end-post.

In order to compare the distribution characteristics of rail displacement on each side of end-post between the two IRJs in vertical direction, the maximum value of a single peak caused by each wheel in Fig. 8(a) is firstly obtained, and then all the peaks information is comprehensively discussed by box diagram (Fig. 9), in which both sides of rail peak displacement distribution of endpost can be clearly seen. The legend in Fig. 9 is that overall mean value, median (middle value when the data are arranged in sequence, which is not affected by outlier data), 1.5IQR data distribution range (edge line of data distribution), and 25%-75% (upper and lower quartiles).

Fig. 9 shows that the rail displacement along wheel side is smaller than towards wheel side in the vicinity of new IRJ end-post, while the state of damaged IRJs is just the opposite, shows that the displacement along wheel side is larger than towards wheel side.

The displacement difference on both sides of the new IRJ endpost is defined asΔh_n, while the damaged IRJ asΔh_b and the mean value of$\Delta \bar{h}_n$and$\Delta \bar{h}_b$is median difference of the distribution. Fig. 9 illustrates that$\Delta \bar{h}_n = 0.2$mm,$\Delta \bar{h}_b = 0.24$mm and the displacement difference of the damaged IRJ is 16.7% larger than the new IRJ. Because of displacement on both sides of end-post in vertical direction exists height differences, leading to wheel-rail generated two different impact modes, one is downward height difference impact and the other is upward height difference impact(Fig. 10) [23,24].

The impact velocity of the new IRJ caused by downward height difference is

$$v_n = \frac{m_{eq}}{m_w}\sqrt{2g\Delta h_n} = 4.47\frac{m_{eq}}{m_w}\sqrt{\Delta h_n} \tag{1}$$

The impact velocity of the damaged IRJ caused by upward height difference is

$$v_b = \frac{m_{eq}}{m_w}v\sqrt{\frac{2\Delta h_b}{R}} = 2.18v\frac{m_{eq}}{m_w}\sqrt{\Delta h_b} \tag{2}$$

Where R is wheel radius of wagon C$_{80}$, whose value is 0.42 m, g is the gravity acceleration, whose value is 9.8 m/s^2.$m_w$is wagon wheel mass,m_{eq} is track equivalent impact mass and v is running speed.
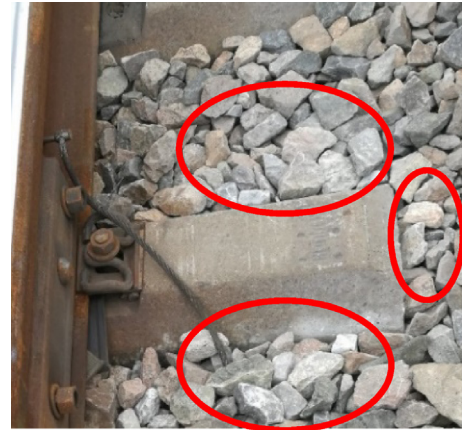
Fig. 12. Partial void under sleepers.
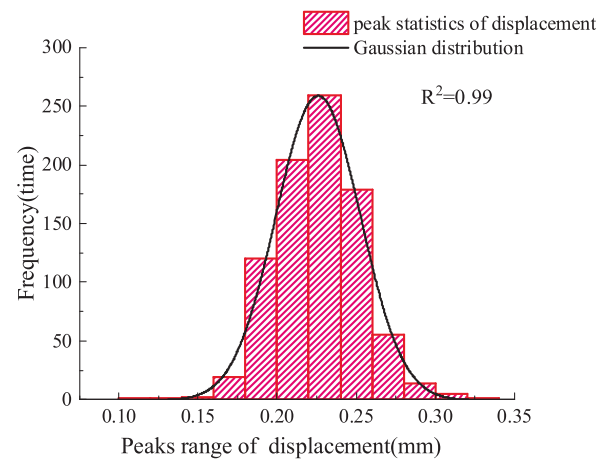
(a)Peaks distribution of sleeper at the new IRJ
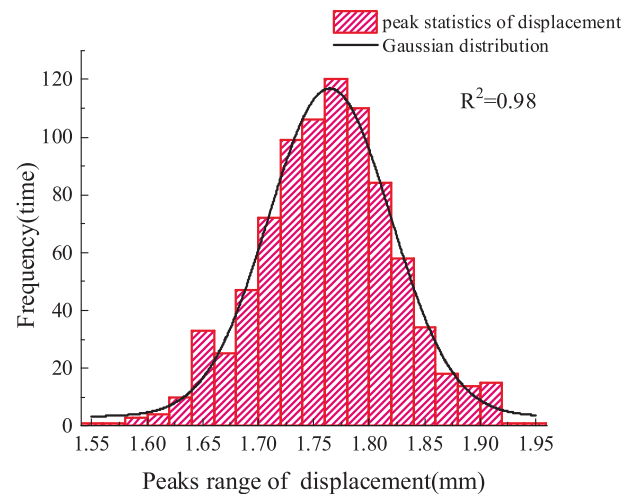
(b) Peaks distribution of sleeper at the damaged IRJ

Fig. 13. Peaks distribution of the two IRJs displacement.

Combing $\Delta \bar{h}_n = 0.2$mm,$\Delta \bar{h}_b = 0.24$mm and Eq. (1)(2), the impact velocity of the new IRJ and damaged IRJ can be obtained, whose results are $v_n = 0.06\frac{m_{eq}}{m_w}$ and $v_b = 0.26\frac{m_{eq}}{m_w}$. Due to $\Delta \bar{h}_n, \Delta \bar{h}_b$

Fig. 14. Typical frequency spectrum of rail.

(a)Influence of speed on rail displacement at the new IRJ

$y_{N2}=3.19-1.45e^{(-x/38)}$

$y_{N1}=2.89-1.44e^{(-x/39)}$

(b)Influence of speed on rail displacement at the damaged IRJ

$y_{B1}=2.97-1.8e^{(-x/37.3)}$

$y_{B2}=0.66+0.15x-0.006x^2+(9.3E-5)x^3$

Fig. 15. Comparison of displacement transfer functions at the two IRJs.

$y=0.11x^{0.24}$

$y=0.19+0.002x$
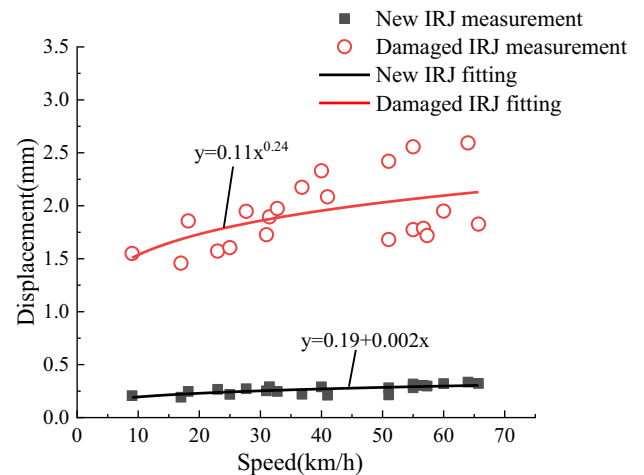
(c) Comparison of vehicle speed to sleeper vertical displacement

Fig. 16. The influence of speed on the displacement of track at the two IRJs.

represent the average value of height difference of the two IRJs, the impact velocity of damaged IRJ is 4.3 times large than new IRJ on average.

There is a dynamic height difference between both sides of end-post which leads to two different impact modes when a wheel passes over the end-post, while the impact mode of upward height difference caused by damaged IRJ has a greater impact on wheel and rail, a stronger destructive effect on the whole track as well.

4.2. Comparative analysis of sleeper displacement

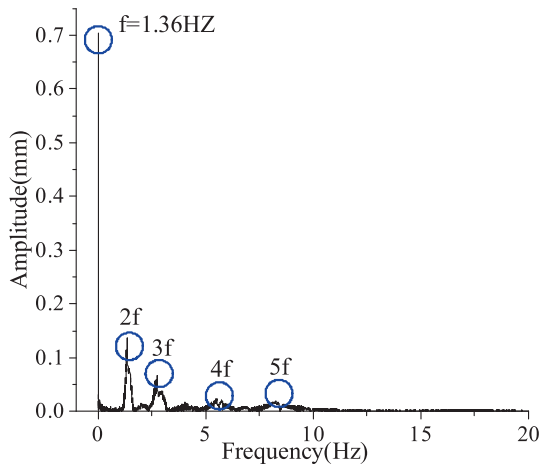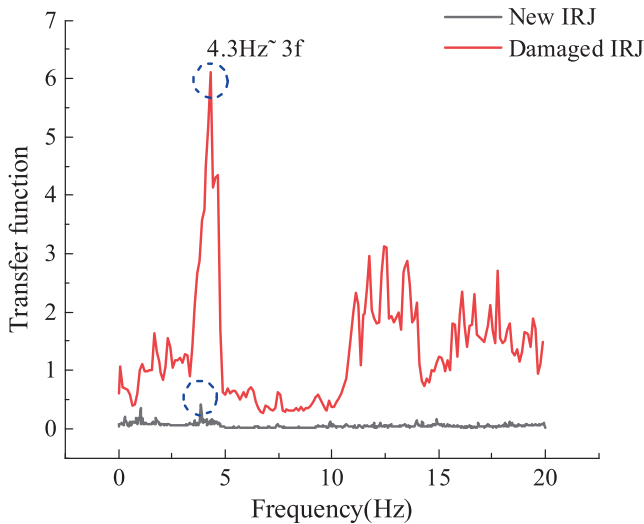Setting the vertical displacements of sleepers at the two IRJs in a same figure, it can be obtained peak values of sleeper displacement (Fig. 11), only a period of time-domain comparison data is shown.

It can be found from Fig. 11 that the sleeper displacement of damaged IRJ is distinct larger than that of new IRJ. The maximum and average values of peaks at new IRJ are 0.32 mm and 0.23 mm, while those at damaged IRJ are 1.95 mm and 1.76 mm. The maximum and average values at damaged IRJ are 6.1 times and 7.65 times higher than new IRJ. The sleeper displacement can reveal wheel-rail impact on one hand, and on the other hand it can reflect the ballast state. The main reason why the displacement of sleeper at damaged IRJ are so large is that the poor regularity of the rail

surface at damaged IRJ, resulting in huge vibration and impact, another reason may be that in the long-term dynamic impact force, causing the ballast broken and pulverized (Fig. 12), leading to void between sleeper and track bed.

(a) Train-track vertical relationship   (b) Connection of each part of the car body
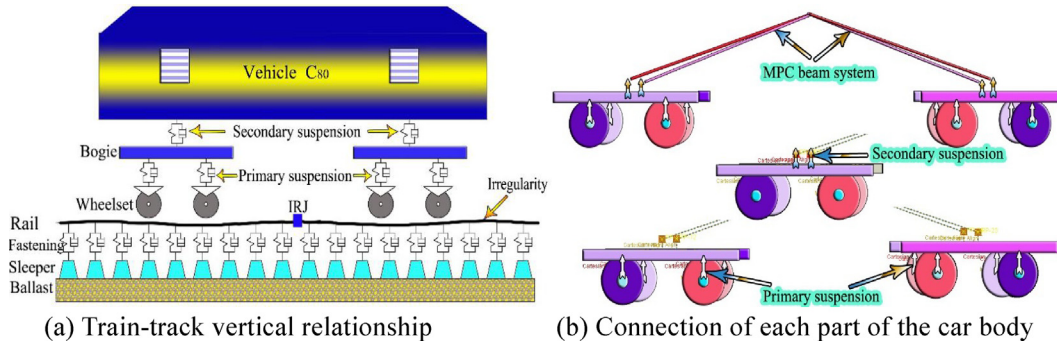
Fig. 17. Vehicle-track coupled model.

From time domain distribution of sleeper displacement, it can be observed that each peak are not completely same, but presents a certain random variation. In order to explore the distribution, peaks of each wheel passing through the IRJs is statistically collected, and the distributions of sleeper displacement in the two IRJs are fitted by the Gaussian distribution (Fig. 13), whose equation is shown in Eq. (3). Fig. 13 shows that the peaks distribution in new IRJ is concentrated between 0.1 and 0.35 mm, while that at damaged IRJ is relatively scattered between 1.55 and 1.95 mm.

$$f(x) = A_0 + Ae^{\frac{-(x-\mu)^2}{2\sigma^2}} \qquad (3)$$

where $A = 1/\sigma\sqrt{2\pi}, \mu$ is the mean, σ is the standard deviation.

4.3. Transfer characteristics of track

Owing to ballast is a complex 3D structure and the motion state of track is not only related to its geometric feature and regularity, but also to the structural performance of each component, such as rigidity of fasteners and ballast. Thus, it is difficult to use one mathematical model to evaluate the influence of joints damage and its service state, because there are many influencing parameters and their effects on the system have nonlinear characteristics. Transfer function is a frequency domain description to express the vibration transfer characteristics of the entire structure, whose mathematical equation can be obtained from input-output relationship of the system(Eq.(4)) [25].

$$H(\omega) = \frac{\frac{1}{2\pi}\int_{-\infty}^{+\infty}Y(t)e^{-j2\pi\omega t}dt}{\frac{1}{2\pi}\int_{-\infty}^{+\infty}X(t)e^{-j2\pi\omega t}dt} = \frac{Y(\omega)}{X(\omega)} \qquad (4)$$

Where $H(\omega)$ is vibration transfer function; $X(t), Y(t)$ is input and output time-domain signals; $X(\omega), Y(\omega)$ is input and output frequency-domain signals.

Before calculating transfer function of the system, frequency spectral feature of the displacement was been analyzed at first. Taking the new IRJ rail data as an example, the typical time-domain diagram of rail displacement is transformed by FFT to obtain its frequency spectrum distribution (Fig. 14).

Since the wagon physical parameter is known, when a train passed through IRJs, it will cause a series of fixed frequencies. Frequency(f)is mainly related to vehicle speed(v)and wavelength(L), whose relationship can be expressed as $f = v/L$. On the basis of wheelbase, adjacent wheelbase, distance of bogie and length of car-body in Section 2.2, they can be substituted into the f equation to get each frequency, whose value is 1.39 Hz, 2.03 Hz, 9.11 Hz and 8.46 Hz.

Fig. 14 shows that the major frequency spectrum peaks of rail are distributed between 0 and 20 Hz, with the maximum spectrum peak f = 1.36≈1.39 Hz, and there are periodic frequencies of 2f, 3f, 4f and 5f in the spectrum distribution. The main vibration spec-trum of rail is consistent with the frequency formed by the train length.

Taking displacement of rail as the input and displacement of sleeper as the output, then transferred time-domain data to frequency-domain data by FFT, finally combing Eq.(4) and input and output data, the transfer function of rail-sleeper at the two IRJs is been calculated(Fig. 15).

Fig. 15 shows that the displacement transfer function from rail to sleeper at the damaged IRJ is distributed between 0.42 and 6.1, while in the new IRJ is 0 to 0.4. The transfer function of the damaged IRJ is obviously larger than the new IRJ, and there is a peak in the transfer function of the two IRJs near 4.3 Hz≈3f, which are 6.1 and 0.4 respectively, in which peak of damage IRJs is 15.3 times larger than new IRJ. Due to the concave of damaged IRJ, its service state of foundation became worse under long-term dynamic wheel load. Especially, the quality of ballast became worse, resulted in transfer function between rail and sleeper has a significant disparity.

4.4. Influence of vehicle speed

In order to analyze the influence of speed on vertical displacement of track at the two IRJs, the maximum displacement in range of operating speed from 10 km/h to 70 km/h was been counted and trend fitted (Fig. 16).

Fig.16(a)shows that rail displacement at N1 and N2 positions on both sides of the new IRJ increasing in an exponentially mode. When speed is 20 km/h, displacement difference between the two sides of the end-post is 0.31 mm, when speed is 70 km/h, the difference is 0.3 mm. Therefore, with the increase of speed, the displacement changes on both sides of end-post is almost unchanged, and displacement on the right side is larger than that on the left side on the whole.

Fig.16(b)shows that, as for the damaged IRJs, the displacement of rail at position B1, goes up exponentially with the speed, while the displacement at position B2, increasing in a cubic polynomial mode. Displacement between the two sides is highly close at lower speed(15–35 km/h). The rail displacement at position B2 changes from decreases to increases between speed in 35–75 km/h, and the difference between both sides of the end-post also raises accordingly. Owing to the vertical difference on both sides of the end-post and rail deformation, leading to a big difference on both sides of the end-post, especially at higher speed of 35–75 km/h. The rail displacement on both sides of the end-post is quite different, giving rise to the increase of wheel-rail dynamic impact.

Fig.16(c)shows that the sleeper displacement of the new IRJ increases linearly with increase of speed, while the damaged IRJ increases nonlinearly. At the same time, it can be got that the difference between the two IRJs goes up with the increase of speed.
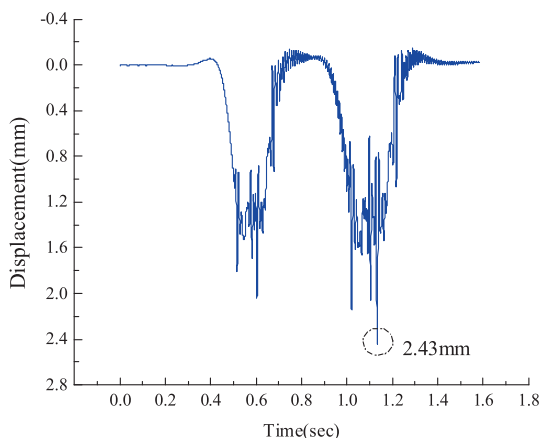
(a) Mesh size=5mm
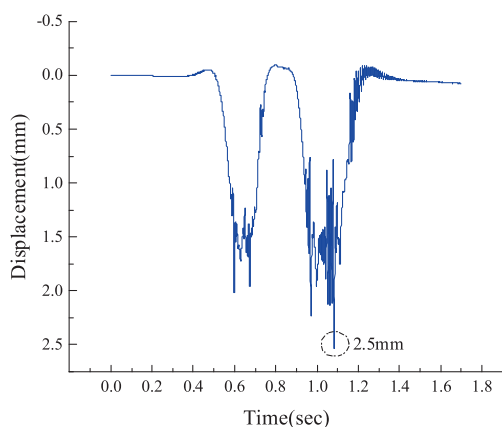
(b) Mesh size=8mm

(c) Mesh size=10mm

Fig. 18. Influence of different mesh size at the damaged IRJ.
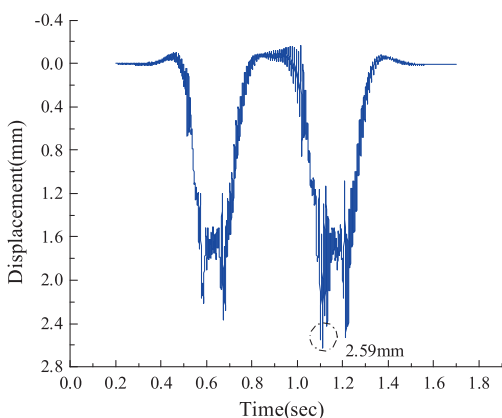
For example, when speed increases from 15 km/h to 70 km/h, the difference changes from 1.3 mm to 1.81 mm.

On the whole, the vertical displacement of rails and sleepers in the new and damaged IRJ rises with the increasing of speed. Speed has obvious influence on the rail displacement distribution on both sides of IRJs.

5. Numerical simulation Analysis5.1Model establishment

In model, the vehicle is a heavy-haul C_{80} wagon. The vehicle model is established based on multibody dynamics theory, which is simplified as one car body, two bogies and four wheelsets. The vehicle and bogies are connected by secondary suspension, and bogies and wheelsets are connected by primary suspension[26]. The suspension systems are simulated by spring-damping units (Fig. 17).In order to let car body, bogie and wheelset to form a 3-D coupling system, utilizing the MPC beam system to connect the each part(Fig. 17(c)).Considering the nonlinear stiffness characteristics of the two suspensions, all parts of the vehicle are regarded as rigid bodies in the model, ignoring their elastic deformation[27].The rolling angle, pitching angle, yawing angle of the vehicle were also been added in the vehicle model.

The track model is based on finite element method, which is consist of rail, fastener, sleeper and ballast, whose paraments is shown in Table2,amoung this, rail, sleeper and ballast are simulated in coarse mesh and 8-node reduced integration element (C3D8R),while the fastener are simulated by spring-damping element and the track gauge is 1435 mm. IRJs are installed in the middle position of longitudinal direction (Z-axis).One meter length plates were modeled on both sides of rail as shown in Fig. 18,the plates are restrained by six bolts. The bolt load Pb was calculated from the bolt torque(T), the bolt diameter(D) and a coefficient (K_b). In the model, T, D and K_b were selected as 1050 N. m,24 mm,0.22, respectively that provided bolt load of 200kN $(P_b = T/K_bD)$[14,28].

There were two different styles of mesh size which were used by other scholars when studying the IRJs. The first one is about 1 mm, which is suitable for the single wheel-rail interaction (Reference [9,10]), not suitable for this model which has eight wheel and a whole train-track system. The second one is about 5 mm-8 mm in the adjacent of IRJ which was been used calculated the static train load (Reference [11,18]). In this case, considering the efficiency and accuracy, before calculation, mesh size 5 mm,8mm,10 mm was been tried and compared with the field test, the result shows blow (Fig. 18).

Compared the field test (Fig. 16(b) shows the field test result of IRJ in R2 is 2.38 mm when speed is 60 km/h) and calculation results (Fig. 18), it can be obtained that when rail mesh size adjacent of IRJ is 5 mm,8mm, the difference between the calculated value and the test value is within 5%, while mesh size 10 mm is more than 5%. Mesh size 5 mm would use up 35 h to calculate (CPU is 128 cores), while mesh size 8 mm only use up 18 h, so balance the efficiency and accuracy of contact solutions, the mesh size 8 mm is been selected for the follow analysis.

A refined mesh (Fig. 19(b)) with maximum size 8 mm was applied in the end-post and in the rail section adjacent to the IRJ (600 mm on both sides of the end-post). The majority of other normal rail mesh size is 0.15 m, the tetrahedral or wedge elements with triangular faces, which have indeterminate contact condition at the corners, are not suitable for analyzing contact problems and should be avoided by remeshing the model [29].

Track irregularity includes track random irregularity and IRJ irregularity. Since China has not launched a standard track spectrum to describe the irregularity of heavy-haul railway, the American five-level spectrum matched with the calculated conditions, thus, it is been applied in the calculation to analyze track random irregularity. IRJ irregularity is employed the measured regularity which is shown in Fig. 5. The established coupled model of heavy haul train-IRJ is shown in Fig. 19.
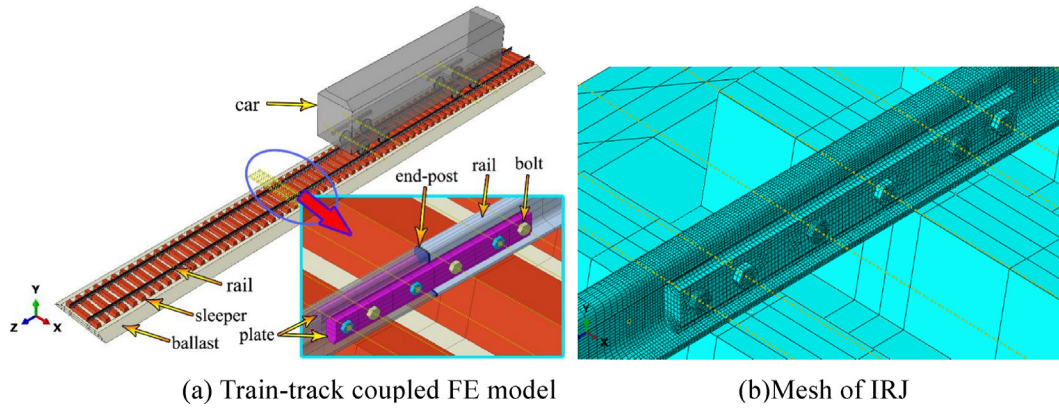
(a) Train-track coupled FE model   (b)Mesh of IRJ

Fig. 19. Finite element model of vehicle-IRJ.

Table 1
Vehicle parameters.

Parameters	Notation	Unit	Magnitude
Mass of car body	Mc	t	91.4
Mass of bogie	Mt	t	1.242
Mass of wheelset	Mw	t	1.257
Vertical stiffness of primary suspension	K_{1z}	MN/mm	160
Vertical damping of primary suspension	C_{1z}	kN.s/mm	4
Vertical stiffness of secondary suspension	K_{2z}	MN/mm	4.89
Vertical damping of secondary suspension	C_{2z}	kN.s/mm	50
Radius of car	R_w	m	0.42

Table 2
Parameters of track.

Name	Parameter	Density (kg/m^3)	Young's Modulus	Poisson's Ration
Rail	CHN75, Length 43.2 m	7850	210GPa	0.3
Plate	Length is 1 m,6 bolt	7800	200GPa	0.3
Sleeper	Concrete,2.6 m × 0.26 × 0.22 (length, width, hight)	2520	38.3GPa	0.2
End-post	Fibre-glass, thickness is 6 mm	1200	4.5GPa	0.19
Ballast	43.2 m × 4.5 m × 0.4 m(L,W,H)	2400	200 MPa	0.25

5.1. Material parameters

The parameters of vehicles and track are shown as Table 1 and Table 2.

The fastener is simulated by spring-damping element, whose vertical stiffness and damping is 100MN/m and 6×10^4n·s/m and the sleeper spacing is 0.6 m[30,31].

5.2. Contact relationship and boundary conditions

The transmission of dynamic force between vehicle and track is mainly solved by wheel-rail interaction, therefore, the key to dynamic FE analysis is to accurately define wheel-rail contact [32]. In this paper, the nonlinear Hertz rolling contact theory is employed to calculate normal wheel-rail contact, and the normal contact force is calculated according to the following formula (5) [33]:

$$P(t) = [\frac{1}{G} \Delta Z(t)]^{3/2}$$ (5)

where G is wheel-rail contact constant (m/N$^{2/3}$),$\Delta Z(t)$ is elastic compression (m) between wheel and rail. Wheels are generally a kind of wear tread, whose calculation formula is$G = 3.86R^{-0.115} \times 10^{-8}(m/N^{2/3})$.

The tangential force of wheel and rail takes use of the Coulomb friction law and penalty approach [34], whose formula is [35,36].

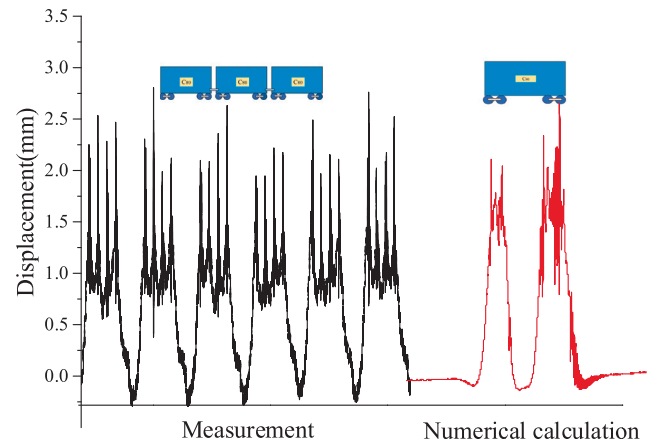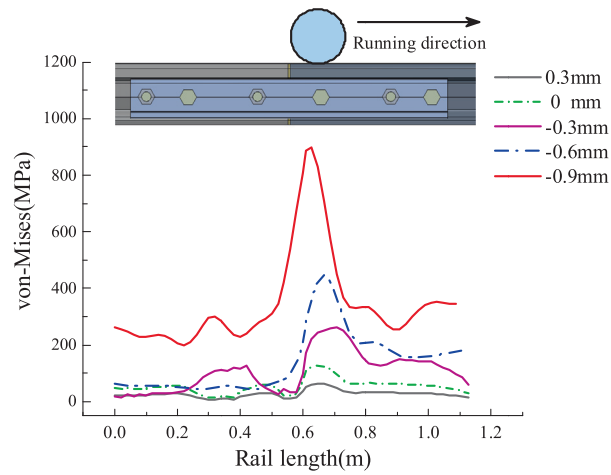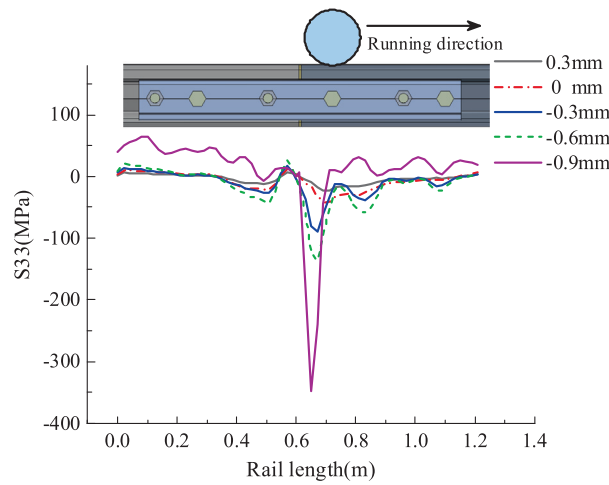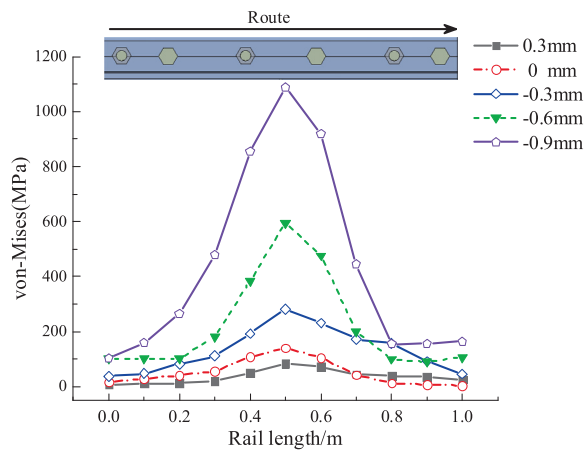$$f^* = f_{cT}^t - k\Delta e$$ (6)

Fig. 20. Verification of numerical simulation results.

(a)Von-mises distribution on the rail-surface in different dipped depths

(b) Tensile stress(S33) distribution on the rail-surface in different dipped depths

(c)Stress distribution of plate in different dipped depths

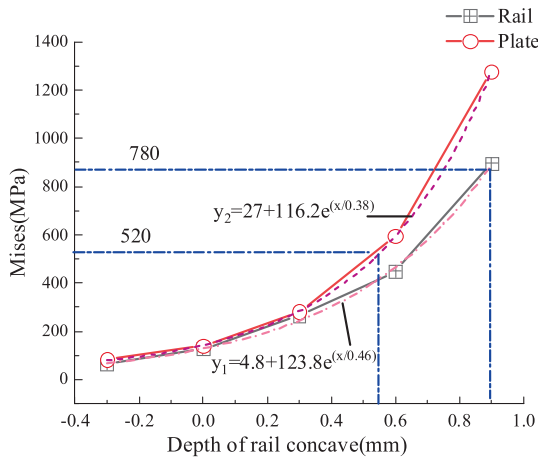**Fig. 21.** Influence of different concave depths on rail and plate stress distribution.

Fig. 22. Influence of concave depth on maximum stress of rail and plate.

Where f^* is trail tangential contact force at time t + 1,k is the penalty contact stiffness,$\Delta e$is the incremental movement of slave node in the FE model.

$$f_{cT}^{t+1} = \begin{cases} f^* & \text{if}|f^*| \leqslant \mu f_{cN}^{t+1} \\ \mu f_{cN}^{t+1} \frac{f^*}{|f^*|} & \text{if}|f^*| \succ \mu f_{cN}^{t+1} \end{cases} \qquad (7)$$

Where f_{cN}^{t+1} is trail normal contact force at time t + 1,$\mu$is the coefficient of friction,0.3.

Rail is be bound with plate and insulating end-plate. The ballast is considered as a linear elastic body, and binding constraint is adopted between sleeper and ballast. At the bottom of ballast, boundary conditions are imposed to limit the displacements in directions × ,y and z. Boundary conditions are imposed to limit the longitudinal (direction z) displacement on both ends of the rail and ballast.

There are two explicit dynamic calculation steps in the FE model, the first one is a balance step which let the vehicle free falling under itself weight, eventually the wheels and rails will contact and train and track system would reach a relatively stable and balanced state. The second one is the running step in which the train would move forward along the track line.

5.3. Result analysis

The correctness of the simulation is verified by combining the simulation results with the field test result (Fig. 20).

Fig. 20 shows that the simulation result is very close to the field test result, thus proving the reliability of the calculation results.

5.3.1. Influence of different dipped depths

For further discuss on the wheel-rail interaction when IRJs existed different dipped depths, established a 3D heavy haul train-IRJ coupled dynamic model by utilizing the FE analysis method.

For obtained the effect of dynamic wheel-rail force in different concave depths, five conditions of 0.3 mm, 0 mm, −0.3 mm, −0.6 mm and −0.9 mm are calculated respectively, among which −0.9 mm is the largest data of all damaged IRJs measured in the field, '+'means convex IRJ, '-'means concave IRJ(Fig. 21).

Fig. 21 shows that the stress distribution of rail and plate are the smallest under the condition of 0.3 mm in convex, which is larger than 0 mm and other concave conditions, reflected that the service state of convex IRJs is better than concave IRJs. It also can be obtained that with the increasing of concave depths, overall stress distribution of rail and plate shows an increasing trend. When the
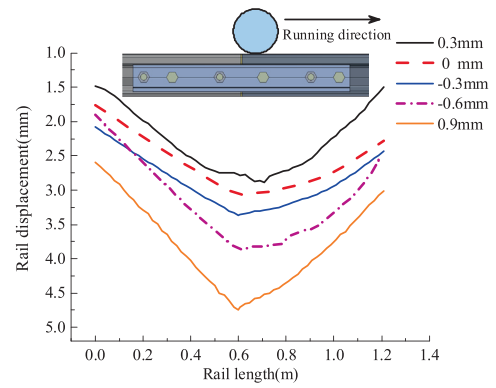
(a)Variation of rail vertical displacement with different concave depths
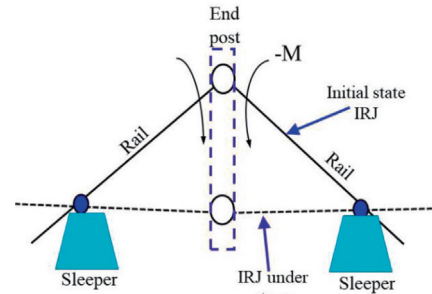
(b)Comparison of convex joint before and after loading
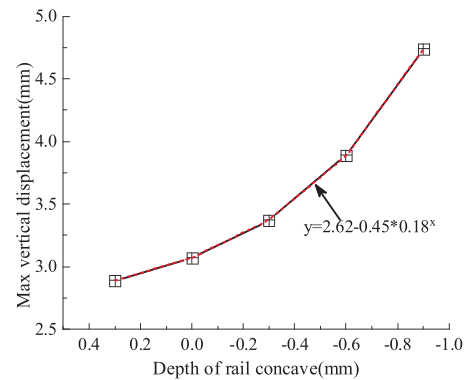
(c)Influence of concave depth on maximum displacement of rail

Fig. 23. Influence of concave depths on vertical deformation distribution of rail.

depth reaches 0.9 mm, the distribution of maximum mises stress, tensile stress of rail and plate suddenly changes, and the service state of IRJ is the worst. Damages such as railhead shelling, fatigue cracking, plastic deformation and fracture of plate are mainly caused by the large stress concentration near the end-post. Therefore, from the point of view to reduce the stress concentration, it is suggested that when installing the IRJs to keep a convex height of 0.3 mm is more appropriate.

The stress peaks of rail and plate corresponding to different depths are plotted in the same figure to obtain the influence relation (Fig. 22). Two blue lines represent the yield stress of plate and rail, which are 520 MPa [22]and 780 MPa[5,6] respectively.

Fig. 22 shows that within the same range of depth, when the maximum yield stress of plate reaches 520 MPa, the maintenance control standard is 0.55 mm; as the rail reaches its maximum yield stress of 780 MPa, the standard is 0.85 mm. Considering the stress limit of fatigue damage easily happened in rail and plate, the stan-
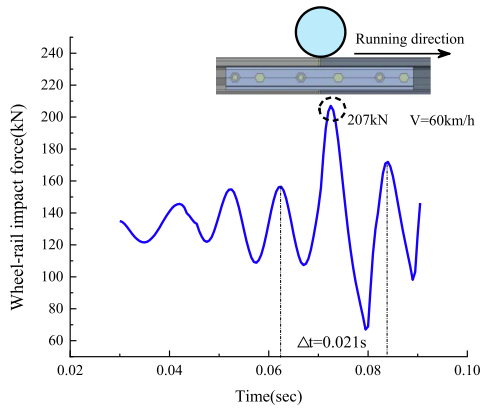
(a)Wheel-rail impact force when speed is 60km/h
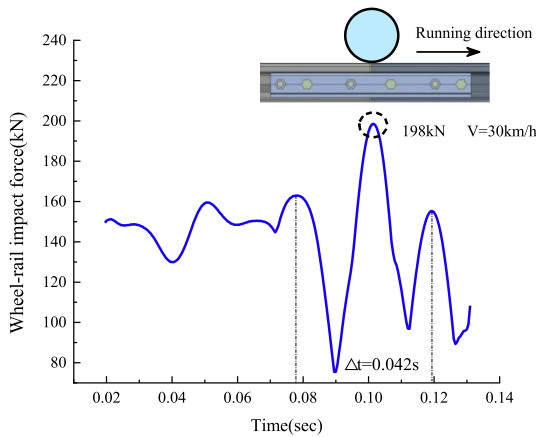
(b)Wheel-rail impact force when speed is 30km/h

$F(x)=60.5+18.3x-0.8x^2+0.014x^3$

(c)Wheel-rail impact force when speed is from 10km/h to 60km/h

Fig. 24. Influence of speed to the wheel-rail impact force.

dard of 0.55 mm is taken as the major maintenance control limit of IRJs concave damage.

For further studying the influence of depths on the vertical deformation of rails, the deformation of rails adjacent IRJs in different ranges of depths are calculated (Fig. 23)

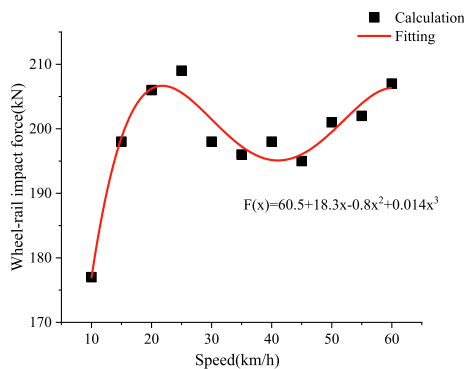Fig. 23(a) illustrates the vertical deformation of IRJ with 0.3 mm convex is the smallest, and the deformation of rail at IRJs with concave is larger, the greater of concave depths, the larger of the rail deformation. When the depths of rail became 0.9 mm, the vertical deformation of rail changes abruptly, whose phenomenon can be

solved by Fig. 23(b). When the IRJ is convex, rails on both sides of the end-post bend downward under the wheel load, and the rail surface is close to straight; however, when the IRJ is concave, the rails on both sides of the end-post continue to bend downward and the regularity of the rail surface becomes worse. Therefore, it is suggested the IRJs should be kept convex when they are installed.

It can be seen from Fig. 23(c) that the maximum displacement of rail increases exponentially with the concave depth of IRJs.

5.3.2. The influence of different speed

From section 4.4 Fig. 16, it can be got that when a train pass over the damaged IRJ, rail displacement and speed show a nonlinear trend, so in order to reveal the phenomenon, calculated the wheel-rail impact force when train speed range from 10 km/h to 60 km/h(Fig. 24).

Fig. 24(a)(b) shows that when train speed is 60 km/h, the Max force is 207kN and $\Delta t = 0.021$s(which can reflect the max impact force duration). When speed is 30 km/h, the Max force is 198kN and the $\Delta t = 0.042$s.

Fig. 24(c) shows that when speed is in the range of 10 to 25 km/h, the impact force increases with the increase of speed, when speed is in the range of 25 to 40 km/h, the impact forces decrease with the increase of speed, while speed is in the range of 40 to 60 km/h, the impact forces increase with the increase of speed. In the general, speed and impact force presented a cubic nonlinear function relationship. Combining Fig. 24 and Fig. 16, we can find that the effect of speed on force and displacement is almost consistent. The results are very similar to the existing research results [37–39].

6. Conclusion

Although CWR are widely used all over the world, the utilization of IRJs is inevitable due to track circuit. Currently, the existing literature researches mainly focus on impact, vibration and stress. Thus, in this paper, field test and 3D FE analysis methods are mainly used to explore the deformation distribution performance of IRJs under the long-term wheel-rail impact. The specify conclusions are follows:

(1) Through the field test of the damaged IRJ and new IRJ, it can be found that the new IRJ shows convex, while the damaged IRJ appears concave. Consequently, under the long-term interaction of wheel-rail, the IRJs will gradually change from convex to concave, which will lead to the damages such as concave, rail bending and dipped.

(2) On both sides of the end-post, the damaged IRJ and the new IRJ present two different impact modes, namely, upward height difference and downward height difference impact. When at the normal operating speed, the impact of the damaged IRJ is as 4.3 times lager than the new IRJ on average.

(3) The ballast of IRJs, under the long-term dynamic impact, will easily become void between sleeper and ballast, leading to significant increase of vertical sleeper displacement. The peaks distributions of sleeper displacement at the new IRJ and the damaged IRJ are normal distribution, with the former distributing mainly in 0.1–0.35 mm, while the latter in $1.55 \sim 1.95$ mm.

(4) The displacement transfer function of the damaged IRJ is obviously larger than that of the new IRJs in the range of 0–20 Hz, with the former's distribution is 0.42–6.1 and the latter is 0–0.4. The transfer function reflects the vibration transfer characteristics of overall track, which can be used as an important index to evaluate the service state of IRJs.

(5) At different speeds, the responses of the two IRJs are distinct unlike. With the increase of speed, the trend of rail displacement variation on both sides of the end-post in the new IRJ is basically the same, while in the damaged IRJ is changes little under the speed of 35 km/h and becomes prominent large between the speed of 35 km/h and 70 km/h.

(6) With the increase of the concave depths in the IRJs , the peak stress of rail and plate are more concentrated and all changes in exponentially mode. Considering that the fatigue stress limits of rail and plate, it is suggested to limit the concave depth of rail within 0.55 mm.

CRediT authorship contribution statement

Hong Xiao: Project administration, Funding acquisition. **Guangpeng Liu:** Methodology, Formal analysis. **Dongwei Yan:** Software, Validation. **Yue Zhao:** Software, Data curation. **Jiaqi Wang:** Supervision. **Haoyu Wang:** .

Declaration of Competing Interest

The authors declare that they have no known competing financial interests or personal relationships that could have appeared to influence the work reported in this paper.

Acknowledgements

References

[1] N.K. Mandal. FEA to assess plastic deformation of railhead material damage of insulated rail joints with fiberglass and nylon endposts[J].Wear.366(2016)3-12.

[2] N.K.Mandal, R. Lewis, Z.F. Wen. Quantification of sub-surface railhead material damage due to composite endpost materials of insulated rail joints for cyclic wheel loadings[J].Engineering Failure analysis.113(2020)104562.

[3] Z.F. Wen, X.S. Jin, W.H. Zhang, finite element analysis of contact-impact of wheel /rail at rail gap, Tribology. 03 (2003) 240–244.

[4] N.K. Mandal, Finite element analysis of the mechanical behavior of insulated rail joints due to impact loadings, Proc IMechE Part F: J Rail and Rapid Transit. (2014) 1–15.

[5] N.K. Mandal, On the low cycle fatigue failure of insulated rail joints, Eng. Fail. Anal. 40 (2014) 58–74.

[6] N.K. Mandal, M. Spiryagin, M. Berg, S. Stichel, On the railhead material damage of insulated rail joints: Is it by ratchetting or alternating plasticity, Int. J. Fatigue 128 (2019) 105197, https://doi.org/10.1016/j.ijfatigue.2019.105197.

[7] Emrecan S, Korhan C. Influence of Track Variables and Product Design on Insulated Rail Joints[J].Transportation Research Record. 2545(2016)1-10.

[8] Y.-C. Chen, L.-W. Chen, Effects of insulated rail joint on the wheel/rail contact stresses under the condition of partial slip, Wear 260 (11-12) (2006) 1267–1273.

[9] Z. Yang, A. Boogaard , Z.L. W ,et al. Numerical study of wheel-rail impact contact solutions at an insulated rail joint[J].International Journal of Mechanical Sciences.138(2018)310-322.

[10] Z .Yang, Anthonie. B,R. Chen, et al. Numerical and experimental study of wheel-rail impact vibration and noise generated at an insulated rail joint [J]. International Journal of Impact Engineering.113(2018)29-39.

[11] M. Gallou, M. Frost, A.E. Hamalawi, et al., Assessing the deflection behavior of mechanical and insulated rail joints through finite element analysis, Proc IMechE Part F: J Rail and Rapid Transit. 232 (09) (2018) 2290–2308.

[12] S. Kaewunruena, C. Chiengson, Railway track inspection and maintenance priorities due to dynamic coupling effects of dipped rails and differential track settlements, Eng. Fail. Anal. 93 (2018) 157–171.

[13] J. Sandstrom, A. Ekberg, Numerical study of the mechanical deterioration of insulated rail joints, Proc IMechE Part F: J Rail and Rapid Transit. 223 (03) (2009) 265–273.

[14] N.N. Zong, D. Wexler, M. Dhanasekar. Structural and material characterisation of insulated rail joints[J]. Electronic journal of structural engineering.13(1) (2013)75-87.

[15] H. Askarinejad, M. Dhanasekar, P. Boyd, R. Taylor, Field measurement of wheel–rail impact force at insulated rail joint, Exp. Tech. 39 (5) (2015) 61–69.

[16] H. Askarinejad, M. Dhanasekar, C. Cole. Assessing the effects of track input on the response of insulated rail joints using field experiments[J]. Proc IMechE Part F:J Rail and Rapid Transit [J].227(2) (2012)176-187.

[17] A. Mayers, The effect of heavy haul train speed on insulated rail joint bar strains, Aust. J. Struct. Eng. 18 (3) (2017) 148–159.

[18] M. Gallou, B. Temple, C. Hardwick, et al., Potential for External Reinforcement of Insulated Rail Joints. . Proc IMechE Part F: J Rail and Rapid, Transit. 232 (03) (2018) 697–708.

[19] M. Oregui, M. Molodova, A. Nunez, et al., Experimental investigation into the condition of insulated rail joints by impact excitation, Exp. Mech. 55 (2015) 1597–1612.

[20] M. Molodova, M. Oregui, A. Nunez, et al., Health condition monitoring of insulated joints based on axle box acceleration measurements, Eng. Struct. 123 (2016) 225–235.

[21] Y.P. Xu. Research on improved rail joint for heavy haul railway[J]. China Railway Science.8(01) (2017)22-28(In Chinese).

[22] TB/T 2975-2018,Bonded insulated rail joints[S]. State Railway Administration of China(In Chinese).

[23] W.M. Zhai. Vehicle-Track Coupling Dynamics(Third Edition) [M].Beijing: China Science Press.2007(In Chinese).

[24] X.W. Yang, G.T. Shi, X.A. Zhang. Generation mechanism of wheel /rail impact noise due to a train wheel passing through rail joints with height difference[J]. Journal of Vibration and Shock.32(17) (2013)59-63(In Chinese).

[25] W C Zhang, Q Su, T Liu,et al. Research on vibration characteristics of ballastless track subgrade under frost boiling at subgrade bed[J]. Rock and Soil Mechanics. 35(12) (2014)3556-3562+3568(In Chinese).

[26] X.P. Cai, Q.H. Wang, D.C. Li, et al., Theoretical study of long elastic sleeper track to reduce vibrations induced by subway trains, Proc IMechE Part F: J Rail and Rapid Transit. 234 (5) (2020) 538–549.

[27] A Miri, M Dhanasekar, D Thambiratnam. Analysis of buckling failure in continuously welded railway tracks[J].Engineering Failure Analysis. 119(2021) 104989.

[28] Mosab Reza Tajalli, Jabbar-Ali Zakeri, Numerical-experimental study of contact-impact forces in the vicinity of a rail breakage, Eng. Fail. Anal. 115 (2020) 104681, https://doi.org/10.1016/j.engfailanal.2020.104681.

[29] K. Hibbitt, Sorensen., ABAQUS/Explicit: user's manual: hibbitt, Karlsson and Sorenson Incorporated (2001).

[30] Y. Sarikavak, O.S. Turkbas, C. Cogun, Influence of welding on microstructure and strength of rail steel, Constr. Build. Mater. 243 (2020) 118220.

[31] X. Ling, H. Xiao, X.H. Cui, Analysis of mechanical properties of polyurethane-mixed ballast based on energy method, Constr. Build. Mater. 182 (2018) 10–19.

[32] Chen .G , Zhai. W.M. A new wheel/rail spatially dynamic coupling model and its verification[J]. Vehicle System Dynamics.41(2004)301-322.

[33] Liang Ling, Peibin Jiang, Kaiyun Wang, Wanming Zhai, Dynamic interaction between rail vehicles and vibration-attenuating slab tracks, Constr. Build. Mater. 258 (2020) 119545, https://doi.org/10.1016/j.conbuildmat.2020.119545.

[34] P. Wriggers, Finite Element Algorithms for Contact Problems, Arch. Comput. Methods Eng. 2 (4) (1995) 1–49.

[35] R. Weyler, J. Oliver, T. Sain, J.C. Cante, On the contact domain method: A comparison of penalty and Lagrange multiplier implementations, Comput. Methods Appl. Mech. Engrg. 205-208 (2012) 68–82.

[36] Z. Yang, X.Y Deng, Z.L Li. Numerical modeling of dynamic frictional rolling contact with an explicit finite element method[J]. Tribology International.129 (2019) 214-231.

[37] A. Johansson, J.C.O. Nielsen, Out-of-round railway wheels wheel-rail contact forces and track response derived from field tests and numerical simulations, Proc. Inst. Mech. Eng. Part F J. Rail Rapid Transit. 217 (2003) 135–146.

[38] N. Correa, E.G. Vadillo, J. Santamaria, et al., On the non-proportionality between wheel/rail contact forces and speed during wheelset passage over specific welds, J. Sound Vib. 413 (2018) 79–100.

[39] N. Correa, E. G. Vadillo, J. Santamaria, et al. On the study of train-track dynamic interactions caused by rail welds on discrete supported rails[J].Wear. 314 (2014)291-298.